

1 **A case study of the large-scale traveling ionospheric disturbances in the East**
2 **Asian sector during the 2015 St. Patrick's Day geomagnetic storm**

3 Jing Liu¹, Dong-He Zhang^{1*}, Anthea J. Coster², Shun-Rong Zhang², Guan-Yi Ma³, Yong-Qiang
4 Hao¹, Zuo Xiao¹.

5 1, Department of Geophysics, Peking University, Beijing, China, 100871

6 2, MIT Haystack Observatory, Westford, Massachusetts, USA

7 3, National Astronomical Observatories, Chinese Academy of Sciences, Beijing, China

8

9 **Abstract**

10 This study presents a comprehensive observation of the large-scale traveling ionospheric
11 disturbances (LSTIDs) in the East Asian sector during the 2015 St. Patrick's Day (March 17, 2015)
12 geomagnetic storm. For the first time, 3 dense networks of GPS receivers in China and Japan are
13 combined together to obtain the 2-dimensional (2D) vertical total electron content (VTEC)
14 perturbation maps in a wider longitudinal range than previous works in this region. Results show
15 that a trough of LSTID spanning at least 60° in longitude (80°E-140°E) occurs and propagates
16 from high to lower latitudes around 09:40-11:20 UT. It is followed by a crest of LSTID which
17 shows a tendency of dissipation starting from the East side. The manifestation of the 2D VTEC
18 perturbation maps is in good agreement with the recordings from 2 high-frequency Doppler shift
19 stations and the iso-frequency lines from 8 ionosondes. Then, the propagation parameters of the
20 LSTIDs are estimated by applying least square fitting methods to the distinct structures in the 2D
21 VTEC perturbation plots. In general, the propagation parameters are observably longitudinal
22 dependent. For example, the propagation direction is almost due southward between 105°E-115°E,
23 while it is slightly South by West/East in the West/East side of this region. This feature is probably
24 related to the regional geomagnetic declination. The mean values of the period, trough velocity
25 (V_t), crest velocity (V_c), and wavelength of the wavelike LSTIDs in the studied longitudinal
26 bands are 74.8 ± 1.4 minutes, 578 ± 16 m/s, 617 ± 23 m/s, and 2691 ± 80 km, respectively. Finally,
27 using the VTEC map data from the Madrigal database of the MIT Haystack Observatory, the
28 characteristics of the ionospheric disturbances over the European sector (30°N-70°N, 10°E-20°E)
29 are also studied. The results are very different from those in the East Asian sector in parameters
30 like the occurrence time, oscillation period, and propagation velocities.

31 **Keywords: Geomagnetic Storm; LSTID; GPS TEC.**

32

33

34

1 **1. Introduction**

2 During the geomagnetic storm, the solar wind energy is impulsively or continually injected into
3 the earth polar region and making the atmospheric and ionospheric states deviate greatly from
4 their background levels [Fuller-Rowell et al., 1994]. In general, the response of the ionosphere to
5 the geomagnetic storm is classified by a variety of different features, one of which is the large
6 scale traveling ionospheric disturbance (LSTID) that is the wave-like perturbation mainly
7 propagating equatorward from high latitudes. Traveling ionospheric disturbances (TIDs) are
8 classified into LSTIDs and Medium-scale TIDs and they are considered to be the ionospheric
9 manifestation of the presence of atmospheric gravity waves (AGWs) stimulated by different
10 sources. LSTIDs are mainly caused by Joule heating or Lorenz-drag forcing in the Auroral regions
11 during geomagnetic storm period [Hines, 1960; Richmond and Roble, 1979; Hocke and Schlegel,
12 1996].

13 In earlier years, the acquisition of the continuous evolution of LSTIDs on a global scale was
14 limited by the availability of the ionospheric observations. In order to obtain the propagation
15 characteristics of LSTIDs on a large spatial scale, researchers needed to organize their findings
16 from limited ionospheric observations, for example, the foF2 data from sparsely distributed
17 ionosondes. In the 1980s, the GPS (Global Positioning System) method was introduced into the
18 ionospheric study [Klobuchar, 1986; Lanyi and Roth, 1988; Coster and Gaposchkin, 1989]. With
19 the dense and worldwide distributed GPS receivers, some characteristic ionospheric phenomena,
20 like traveling ionospheric disturbances (TIDs) [Saito et al., 1998; Tsugawa et al., 2004; Ding et al.,
21 2007], ionospheric storms [Ho et al., 1996], and ionospheric responses to solar flares
22 [Afraimovich, 2000a; Zhang and Xiao, 2005] were revisited frequently and new results were
23 obtained.

24 The propagation characteristics of LSTIDs are always topics of great research interest [Hunsucker,
25 1982; Ho et al., 1996; Balthazor and Moffett, 1999; Afraimovich et al., 1998, 2000; Shiokawa et
26 al., 2002; Tsugawa et al., 2003, 2004; Ding et al., 2008, 2014; Borries et al., 2009, 2017;
27 Habarulema et al., 2015, 2016, 2018; Zakharenkova et al., 2016; Figueiredo et al., 2017; Pederick
28 et al., 2017; Cherniak et al., 2018; Lyons et al., 2019]. Based on limited GPS stations
29 measurements, Afraimovich et al. [1998] propose a radio interferometry method to roughly
30 estimate horizontal propagation velocities and phase front angles of TIDs. Further, the world-wide
31 or local dense distribution of the GPS receivers networks facilitates the acquisition of the global or
32 regional TEC perturbation maps with high spatial and temporal resolutions to reveal the detailed
33 propagating characteristics of TIDs [Ho et al., 1996; Saito et al., 1998; Tsugawa et al., 2004;
34 Borries et al., 2009; Ding et al., 2012]. With more than 60 GPS receivers distributed worldwide,
35 Ho et al. [1996] studied the global distribution of TEC variations and perturbations during a
36 magnetically disturbed period. They identified a TID propagating from the northern sub-auroral
37 region to lower latitudes at a speed of about 460 m/s. The GPS Earth Observation Network
38 (GEONET) in Japan is one of the densest GPS receiver networks on the Earth, and utilizing its
39 data two-dimensional (2D) TEC perturbations over Japan can be mapped. With these
40 high-resolution TEC perturbation maps, the spatial structures and temporal evolutions of a TID in
41 the nighttime mid-latitude ionosphere over Japan were revealed clearly [Saito et al., 1998]. Since
42 then, with this dense GPS network, the characteristics of LSTIDs over Japan are carefully studied
43 through case and statistical analysis, and some propagation features of TIDs in this region are

1 revealed [Saito et al., 2001; Shiokawa et al., 2002; Tsugawa et al., 2003, 2004, 2006].

2 For the LSTID with scales of thousands of kilometers, the extensive spatial coverage of
3 ionospheric observations is undoubtedly useful for capturing its propagation features. In recent
4 years, the GPS data from densely distributed GPS stations in China are used to study LSTIDs in
5 this region [Ding et al., 2012, 2013, 2014; Song et al., 2013]. Based on the GPS data from the
6 Crustal Movement Observation Network of China (CMONOC), Ding et al. [2012] obtains
7 temporal continuous 2D imaging of ionospheric disturbances during the geomagnetic storm on
8 May 28, 2011, and find two LSTIDs moving southwestward with the front width of at least 1600
9 km during different storm phases. In addition, through the comparative climatological study of
10 LSTID over North America and China, the different time dependence of LSTID occurrence over
11 two longitudinal sectors were revealed statistically [Ding et al., 2014]. These studies further
12 emphasize the effectiveness of the large coverage, high-resolution ionospheric observations from
13 GPS networks on the detailed investigation of structures of the ionospheric disturbances.

14 The propagating direction of the LSTID during the geomagnetic storm has always been focused
15 on for the LSTID studies. From case and statistical studies about LSTID during geomagnetic
16 storm period over East-Asia region conducted independently by Chinese and Japanese scientists in
17 recent years, the dominant propagating direction of LSTID in China and Japan is a little different.
18 It mainly propagates South by West in the Chinese region [Ding et al., 2014], while it mainly
19 propagates South by East in the Japanese region [Tsugawa et al., 2004]. Although the geomagnetic
20 declination is considered to be one of the main factors to be responsible for the propagation
21 direction of LSTID based on different LSTID studies, the LSTID studies concerning the same
22 geomagnetic storm using both Chinese and Japanese GPS networks together have not yet been
23 reported.

24 During the period of 17–18, March 2015, the strongest geomagnetic storm in the 24th solar cycle
25 occurred and LSTIDs are detected and analysed in different longitudinal sectors [Ramsingh et al.,
26 2015; Borries et al., 2016; Zakharenkova et al., 2016; Habarulema et al, 2018]. Meanwhile, two
27 high frequency (HF) Doppler stations operated by China Meridional Project [Wang, 2010] at
28 mid-latitude China record large ionospheric HF Doppler shifts after 10:00 UT, which seem to
29 indicate the LSTIDs in the Asian region between 09:00-12:00 UT that reported by Habarulema et
30 al. [2018]. In this study, the multi-network of densely distributed GPS receivers, the HF Doppler
31 stations, and an ionosonde network are used to conduct a more comprehensive study on the
32 propagating characteristics of the disturbances in the East Asian region, especially on the
33 characteristics of the dominant propagating direction over China and Japan.

34 **2. Data and Methods**

35 Figure 1 illustrates the locations of ground-based receivers that are used in this study from 4
36 Global Navigation Satellite Systems (GNSS) networks distinguished by colors. They are Chinese
37 Meteorological GNSS Network (CMGN), CMONOC in China, GEONET in Japan, and
38 International GNSS Service (IGS). These receivers are selected through data quality checking and
39 regional restriction ($10^{\circ}\text{N} \sim 60^{\circ}\text{N}$, $70^{\circ}\text{E} \sim 150^{\circ}\text{E}$), and the numbers of used stations are 259, 220,
40 1300, and 31 for CMGN, CMONOC, GEONET, and IGS, respectively. The sample rate of all GPS
41 data is 30 seconds. Combining the carrier phase and pseudo-range measurements in two L-band
42 frequencies of GPS receivers' observations, the vertical TEC can be obtained. In the calculation,

1 the height of the ionospheric thin shell is set to be 400 km, and the cutoff elevation angle is 30
2 degrees. The detailed process of the TEC calculation from GPS data can be found in our previous
3 works [Zhang et al., 2009; Zhang et al., 2010].

4 Different methods have been used for extracting the TEC perturbations related to LSTIDs in
5 previous works [Wan et al., 1997; Afraimovich et al., 2000; Shiokawa et al., 2002; Nicolls et al.,
6 2004; Tsugawa et al., 2004; Ding et al., 2007]. Afraimovich et al. [2000] suggest that the LSTID
7 characteristics in TEC can be determined by removing the trend with 3 to 5 order polynomials in
8 order to eliminate the trends introduced by the motion of satellites and variations of the regular
9 ionosphere. For a similar purpose, Shiokawa et al. [2002] subtract a running average of TEC over
10 1 hour from the raw TEC. With more than 1000 GPS receivers over Japan, a series of 2D TEC
11 perturbation maps can be obtained. Ding et al. [2007] develop another method of obtaining the 2D
12 TEC perturbation maps by expressing the vertical TEC as a one-order function of local time and
13 latitude. According to their argument, this method is sufficient to remove background trends for
14 continuous observation of a GPS receiver-satellite pair without introducing artificial perturbations.
15 After comparing the results of these methods, a method similar to Ding et al. [2007] is conducted
16 in this study, in which the vertical TEC at an ionospheric pierce point (IPP) is treated as a function
17 of universal time (UT), longitude (Lon), and latitude (Lat), i.e.,

$$VTEC_0 = C_0 + C_1UT + C_2Lon + C_3Lat \quad (1)$$

$$VTECP = VTEC - VTEC_0 \quad (2)$$

18 in which $VTEC_0$ is the background change and $VTECP$ is VTEC perturbation. Then, the obtained
19 $VTECP$ data is reorganized into pixels which are bounded by $10^\circ\text{N} \sim 60^\circ\text{N}$, $70^\circ\text{E} \sim 150^\circ\text{E}$ and
20 with a spatiotemporal resolution of 1° longitude \times 1° latitude \times 10 minutes. The $VTECP$ value for
21 each pixel is set to be the average of all $VTECP$ data of which the IPP and UT locate in this pixel.
22 After these steps, the featured ionospheric disturbances are expected to appear on a series of 2D
23 $VTECP$ maps.

24 As a comparison, the VTEC map from Madrigal database of the MIT Haystack Observatory is
25 used to reveal the ionospheric disturbances in the European sector ($30^\circ\text{N} \sim 70^\circ\text{N}$, $10^\circ\text{E} \sim 20^\circ\text{E}$).
26 This database provides worldwide VTEC values in 1° latitude \times 1° longitude pixels with a
27 temporal resolution of 5 minutes [Rideout and Coster, 2006] and has good data coverage in
28 European and American sectors. VTEC maps with such a high spatiotemporal resolution are
29 suitable to reveal the structures of traveling ionospheric disturbances [Zhang et al., 2017].

30 The Doppler shift data observed at two high frequency (HF) Doppler sounding stations in China is
31 collected, of which the station codes are MDT (40.4°N , 116.9°E), and SZT (22.6°N , 114.1°E). The
32 sounding system continuously receives electromagnetic waves with a stabilized frequency of 10
33 MHz transmitted by the National Time Service Center (NTSC) (35.7°N , 109.6°E) to detect the
34 ionospheric disturbances through the Doppler shifts of this standard frequency. These shifts are
35 considered to be caused by ionospheric variations mainly around the reflecting point of the
36 electromagnetic wave in the ionosphere. According to the geometrical relationships, the locations
37 of the reflecting point for MDT and SZT are (38.0°N , 113.2°E) and (29.2°N , 111.8°E), respectively.
38 These stations are marked in Figure 1 with colored stars.

39 In this study, ionograms from 8 ionosonde stations in China middle latitude are used to derive the

1 iso-frequency lines, which vary as a function of universal time and virtual height. The sample rate
2 of the ionograms is 15 minutes. These ionosondes belong to the China Research Institute of
3 Radio-wave Propagation (CRIRP) and their locations are marked in Figure 1 with green triangles.
4 The virtual height data is manually scaled by ourselves to reduce possible errors of auto scaling
5 [Krankowski et al., 2011; Habarulema and Carelse, 2016] from these ionograms with professional
6 scaling software provided by CRIRP. During the scaling, we limited the frequency to be less than
7 7 MHz. In addition, the condition of the geomagnetic storm is shown with data from the high
8 resolution (5 minutes) OMNI dataset, which is downloaded from the FTP service of the NASA
9 Goddard Space Flight Center.

10 **3. Results**

11 **3.1 Observations**

12 Figure 2 shows the variations of (a) solar wind speed, (b) interplanetary magnetic field (IMF) B_z
13 component, (c) the SYM-H index, and (d) the AE index from the OMNI dataset, and the time
14 range is from 18:00 UT, 16 March 2015 to 06:00 UT, 18 March 2015. It should be noted that the
15 solar wind magnetic field and plasma data are time-shifted to the bow shock nose to better support
16 the solar wind-magnetosphere coupling studies. It can be seen clearly that a geomagnetic storm
17 occurred on 17 March 2015, with the sudden storm commencement (SSC) at $\sim 04:45$ UT, which is
18 characterized by a sharp increase (marked with vertical dashed lines) in the solar wind speed, B_z ,
19 and SYM-H index. The main phase of the storm can be roughly divided into two stages. The first
20 stage is from $\sim 06:00$ UT, when the IMF B_z component first turns to southward, to $\sim 12:00$ UT,
21 when the B_z turns southward again after back to northward for about 2 hours. After $\sim 12:00$ UT,
22 the B_z is southward for most of the time, until it enters the recovery phase. The SYM-H and AE
23 indices show a similar two-stage feature as the B_z . SYM-H decreases after $\sim 06:00$ UT, reaches
24 the first minimum at $\sim 09:30$ UT, and increases to a local maximum at $\sim 12:00$ UT. Then, it
25 gradually decreases with small oscillations and reaches the minimum value of -233 nT at $\sim 22:45$
26 UT. Correspondingly, the AE index exhibits the first increase period between 06:00 UT to 12:00
27 UT, with the maximum intensity of ~ 1000 nT, and the second period between 12:00 UT to 02:00
28 UT of the next day, during which the AE increases much larger with several peaks. This storm is
29 the strongest one in the 24th solar cycle [Astafyeva et al., 2015].

30 During the first stage of the main phase, disturbances are observed successively at MDT and SZT
31 Doppler receiver stations. Figure 3 illustrates the variations of the Doppler shift records at (a)
32 MDT and (b) SZT between 08:00 UT and 14:00 UT on 17 March 2015. It shows that two distinct
33 positive shifts occur at about 10:22 UT and 10:53 UT, respectively. Shortly after, it exhibits two
34 negative shifts but with much smaller amplitudes. Suppose these successive disturbances indicate
35 a propagating perturbation, according to the estimated locations of the reflecting points that
36 mention above and the occurrence time of the two positive peaks, the approximate speed of this
37 perturbation is about 535 m/s. This value is much larger than the speed of the movement of the
38 ionospheric negative storm that usually occurs in the middle latitude due to storm-induced
39 equatorward wind [Buonsanto, 1999], and the ionospheric storm is not serious in the Asian sector
40 during this period [Astafyeva et al., 2015]. Considering the magnitude of the speed and the time
41 interval of the positive-negative variations, the recorded perturbations probably reflect an
42 equatorward propagating LSTID in the East Asian sector.

1 To confirm this, Figure 4 presents a sequence of 2D VTECP maps between 09:40-11:40 UT on 17
2 March 2015 with the method described in section 2. The grey areas represent the nightside. The
3 raw value of VTECP has already been converted into VTECP' with the equation

$$\text{VTECP}' = \text{sgn}(\text{VTECP}) * \log_{10}(\text{abs}(\text{VTECP}) + 1) \quad (3)$$

4 The raw amplitude of VTECP above 30°N is ~ 2 TECu while the raw amplitude of VTECP below
5 30°N reaches ~ 10 TECu. So, transform (3) provides a better colormap for 2D VTECP plots by
6 sharpening the edges between positive and negative values and reduce the differences of VTECP
7 in middle and low latitudes. Consequently, it should be noted that the amplitude of the wavelike
8 variation does not represent the true wave amplitude but an “artificial” one. The yellow lines
9 illustrate the least square fitting results for all the negative pixels within certain rectangular areas
10 bounded by longitudes and latitudes. The green lines are similar but for pixels with the bottom 5%
11 absolute VTECP' values in selected areas (see section 3.2 for a detailed example). These two
12 kinds of lines mark the approximate locations of the wavefronts.

13 A large-scale wavelike perturbation can be seen clearly in Figure 4. The first relatively distinct
14 wave structure emerges during the (d) 10:10-10:20 UT period, while its sign can already be
15 observed as early as (a) 09:40-09:50 UT in the northwest part of China. During (e) 10:20-10:30
16 UT, a negative band occurs across both the Chinese and Japanese sectors between around
17 30°N-45°N, which gradually propagates to lower latitudes in the next tens of minutes. During (f)
18 10:30-10:40 UT, the first clear wavefront of the positive band appears, which also shows an
19 equatorward movement for at least half an hour. Finally, there seems to be no distinct wave
20 structure following the positive band. Considering the spatiotemporal characteristics of this
21 perturbation, it can be preliminarily identified as an LSTID. By the way, it is interesting to note
22 that the positive bands do not extend to the Japanese sector in (h) and (i), and the corresponding
23 VTECP' amplitudes seem smaller in the East side than in the West side. This may be related to the
24 fact that the Japanese sector has already entered the nightside.

25 Both the negative and positive bands exhibit more complex variations when they enter the
26 equatorial ionospheric anomaly (EIA) region between 20°N-30°N. On the one hand, the amplitude
27 of VTECP' is relatively larger than those in the higher latitudes. On the other hand, it seems that
28 the equatorward propagation of the negative band decelerates significantly in this area, which is
29 especially shown in (Figure 4, g-l). Such complex features are probably related to the various
30 physical processes in this region. Ding et al. [2012] suggest that LSTIDs experience severe
31 dissipation in South China region due to viscosity and heat conductivity at low latitudes, which
32 may account for the weakening of the equatorward propagating wavelike structures. Besides,
33 Pradipta et al. [2016] studied the interaction of the auroral LSTIDs from opposite hemispheres
34 near the dip equator during the 26 September 2011 geomagnetic storm. It shows that such
35 interaction may bring much complexity to the TEC perturbations near the dip equator.

36 Our observations of the Doppler shift and VTECP' maps are in good agreement. To show it
37 clearly, Figure 5 shows the variations of the mean VTECP' data near the Doppler reflection points
38 with the same time range of Figure 3. Doppler shift recordings in Figure 3 are also plotted with
39 dashed lines for comparison. It can be seen that the troughs at around 10:20 UT in (a) and 10:50
40 UT in (b) correspond well to the two distinct crests in Figure 3. In addition, the variations of the
41 VTECP' between 11:00 and 14:00 are also in a good negative correlation with the Doppler shift

1 observations for each reflecting point. It should be noted that the variation of VTECP' at the
2 reflecting point 1 exhibits more variability than that at the reflecting point 0, especially around
3 09:00 UT, 10:00 UT, and 12:00 UT. Considering that point 1 (29.2°N,111.8°E) is approaching the
4 EIA region, the causes for VTEC perturbations are more complicated as mentioned above. This
5 feature is consistent with the observations of the 2D VTECP' maps in Figure 4.

6 Ionospheric parameters from ionograms have been commonly used since early TID studies.
7 Recently, ionograms and iso-frequency lines with different sampling rates were used in TID
8 studies [Klausner et al, 2009; Ding et al., 2012, 2013; Pradipta et al., 2015; Ramsingh et al., 2015;
9 Habarulema et al., 2018]. Figure 6 presents the temporal variations of the virtual height for each
10 iso-frequency line. The names and locations of the corresponding ionosondes are given in each
11 subplot as annotates. The sampling frequency are marked on the right side for each line. On the
12 left column, the results of five stations are arranged in order from high to lower latitudes, and on
13 the right column, it shows the recordings of four stations in the same latitudinal belt. We can see
14 clearly that a distinct uplift of the virtual height occurs at 09:45 UT at Manzhouli station, and it
15 gradually moves equatorward from high to lower latitudes (Figure 6, a-e). Meanwhile, the phase
16 difference is not observed for the stations on the right column. This means that the ionospheric
17 disturbance roughly moves along the meridian line in this longitudinal sector (around 115°E),
18 which corresponds to the results of the 2D VTECP' map. Moreover, although the time resolution
19 of 15 minutes is relatively low, it can still be identified that the crests in the higher iso-frequency
20 lines appear earlier than those in the lower ones. Such trends (marked with black dashed lines)
21 indicate a downward vertical phase velocity, which is one of the typical characteristics of TID and
22 AGW [Hine, 1960; Hocke and Schlegel, 1996]. It should be noted that the downward trend is not
23 much clear for certain station, especially the one in Qingdao. This may be attributed to the 15
24 minutes sampling interval.

25 3.2 Estimating Propagation Parameters

26 As preparation for estimating the propagation parameters of this LSTID, Figure 7 shows a detailed
27 example of the wavefront fitting method with the VTECP' map in Figure 4(g) (10:40-10:50 UT).
28 The reason for choosing this period is that the structure of the wavefront is relatively clear, and the
29 boundary of the positive and negative wave band in the Japanese sector can still be partly
30 identified. The green line is the least square fitting for the green dots, of which the absolute
31 VTECP' values are close to zero (bottom 5%) among all the dots in a certain region (75°E-140°E,
32 30°N-40°N). The wave propagating azimuth (marked with arrows) can be estimated with the
33 normal direction of this fitting line. Results are listed in Table 1 in the second column.

34 It can be seen clearly that the TID moves due South around 110°E, and in the West/East region,
35 the propagation direction is slightly South by West/East. It should be noted that the morphology of
36 this TID is continuously changing as it moves from high to lower latitudes in the studied region.
37 Although the azimuths are estimated only with the wavefront data during 10:40-10:50 UT, such
38 longitudinal dependence of azimuths corresponds well with other fitting lines in Figure 4(e, f, g,
39 h).

40 In order to derive the phase speed, period, and wavelength of this LSTID, the time-latitude plots
41 (TLPs) of VTECP' are obtained for six longitudinal bands, which are marked with dashed
42 rectangles A-F in Figure 7. For each band, the VTECP' data is averaged along the latitude for

1 every 6 minutes (0.1 hours), and the results as a function of UT and latitude are illustrated
2 correspondingly in Figure 8 (a-f). As mentioned before, the VTECP' variation related to EIA is
3 rather complex. Considering that EIA is mainly a low-latitudinal phenomenon, the 30°N is marked
4 with dashed lines in Figure 8 which indicate the boundary of EIA. Only values over 30°N are used
5 to estimate the speed.

6 As expected, the most distinctive structures in all panels are the pair of negative and positive
7 bands around 10:40 UT, which correspond to the perturbations moving from high to lower
8 latitudes shown in Figure 4. The structures in the 130°E-140°E are not quite clear, which may be
9 due to the lack of data in some parts of this area, but the trough around 10:40 UT can still be
10 identified. To estimate the meridional phase speeds of these perturbation patterns, the linear least
11 square method is used to fit the pairs of troughs and crests. The data points for the linear fitting are
12 marked with white dots, which are the minimum/maximum values along with each latitudinal bin
13 around the negative/positive structures that we focus on. The phase speeds for wave troughs (V_t)
14 and crests (V_c) can be derived based on the slopes of the fitting lines. Moreover, the period of the
15 wave can be estimated through the time interval between the trough and crest in TLPs. In practice,
16 for each longitudinal region, the average of time lags along all latitudinal bins is set to be the half
17 period of the wave in this region. As for the estimation of wavelength, note that the studied area is
18 $\sim 20^\circ$ in latitude, which is roughly one wavelength and thus make it difficult to estimate the
19 wavelength directly from the 2D VTECP' map. So, the wavelength is derived from the
20 multiplication of speed and period.

21 However, those speed, period, and wavelength are the projections on longitudes. After adjusted by
22 the propagation azimuths that were calculated above, the final results of the estimated parameters
23 are listed in Table 1. It can be seen that these parameters show certain longitudinal dependence. It
24 should be noted that the data coverage is relatively lower in the east and west boundaries of the
25 investigated region. This may impact the accuracy of the estimation of the LSTID properties in
26 these areas. Besides, the mean values and standard deviations of the period, V_t , V_c , and
27 wavelength are 74.8 ± 1.4 minutes, 578 ± 16 m/s, 617 ± 23 m/s, and 2691 ± 80 km, respectively. These
28 parameters are typical for an LSTID. V_t and V_c overlap, although only marginally, considering the
29 error ranges. Meanwhile, the mean V_c is slightly larger than the mean V_t , which seems like the
30 wave behind is pushing that ahead. In general, the speed of trough and crest of the LSTID should
31 be rather the same since they are induced by the same gravity wave. However, the wave properties
32 might change with time dependent on the forcing from background condition, especially for
33 LSTID covering large spatial region. This might explain the differences.

34 In addition, it is interesting to note that V_t is in reasonable agreement with the result of 535 m/s
35 derived from the Doppler recordings. To show it more specifically, we estimated the speed and
36 direction of the LSTID using the same TLP method as Figure 8 but in 111°E-114°E and
37 29°N-38°N (corresponding to the reflecting points). The result is 562 ± 59 m/s and 0° , respectively.
38 In general, the LSTID velocity estimated from ground-based stations tend to be larger than the
39 actual velocity since these stations, in most cases, are not in perfect alignment with the
40 propagation direction of the LSTID [Afraimovich et al., 1998; Habarulema et al., 2013]. Such
41 good agreement between VTECP' and HF Doppler results may be attributed to the fact that the
42 reflecting points (29.2°N, 111.8°E; 38.0°N, 113.2°E) of the Doppler receivers are in a narrow
43 longitudinal band and the direction of the LSTID's propagation is also almost due south between

1 111°E-114°E.

2 As mentioned above, the VTECP' in the EIA region seems to exhibit different features compared
3 to that in the middle latitude. It can be seen from Figure 8(c) that VTECP' in this region also
4 shows a periodic variation, but it seems to have longer period and time duration than the LSTID.
5 These disturbances are probably related to the complex variations of VTEC after 08:00 UT
6 (around dusk). Besides, the perturbations at 20°N around 12:00 UT and 13:00 UT show patterns of
7 poleward movement. Habarulema et al. [2018] have identified TIDs in the Asian-Australian sector
8 during the same storm period. It provides clear examples of TIDs crossing the dip equator from
9 the southern hemisphere to the northern hemisphere around 09:00-12:00 UT. Their analysis shows
10 that these TIDs may not have exceeded 30°N. Such poleward feature is also detected in other
11 longitudinal sectors during this storm [Zakharenkova et al., 2016] and other storms [Pradipta et al.,
12 2016; Jonah et al., 2018]. In addition, Ding et al. [2013] have studied the poleward-propagating
13 LSTIDs in southern China during a medium-scale storm in 2011. They attribute their observations
14 to the excitation of secondary LSTIDs during the dissipation of primary disturbances from the
15 lower atmosphere. Besides, the poleward-moving disturbances may also be induced by the
16 variation of the equatorial electrojet as pointed out by Chimonas [1970] and more recently by
17 Habarulema et al. [2016]. A detailed investigation of this phenomenon is not the focus of this
18 work.

19

20 **4. Discussion**

21 Our results show that the propagation parameters of the LSTID in the East Asian sector during the
22 St. Patrick's Day storm are longitudinal dependent. Among these parameters, the longitudinal
23 dependence of the propagation azimuth of an LSTID receives much attention in previous works.
24 In general, earlier studies suggest that there are four main factors that affect the direction of a
25 polar originated LSTID, which are the velocity of the background neutral wind [Hines, 1960;
26 Morton and Essex, 1978; Maeda and Handa, 1980], the structure and evolution of the source
27 region in the auroral oval [Maeda and Handa, 1980; Hunsucker, 1982; Ding et al., 2007], the
28 Coriolis force [Maeda and Handa, 1980; Balthazor and Moffett, 1999; Afraimovich et al., 2000;
29 Tsugawa et al., 2004; Ding et al., 2013], and the declination of geomagnetic field [Tsugawa et al.,
30 2004; Borries et al., 2009].

31 The Coriolis force effect is generally believed to contribute to the clockwise shift of the
32 propagation direction of the LSTIDs [Afraimovich et al., 2000; Tsugawa et al., 2004; Ding et al.,
33 2013], The observations of the shift (10°-20° on average) are consist with the calculation by
34 Maeda and Handa [1980] and the model simulation by Balthazor and Moffett [1999]. However, in
35 our study, the shift of the propagation direction is not systematic westward, which means the
36 variability of the LSTID azimuth in our observation cannot be attributed to the Coriolis force, at
37 least not to it alone.

38 The structure/movement of the source region for the LSTID in the auroral oval is another
39 candidate for explaining the longitudinal dependence of the propagation direction of the LSTID.
40 Previous studies have suggested that the westward movement of enhanced electrojets in the
41 auroral arc is an important cause of the westward shift of the LSTID propagation direction at high

1 latitudes [Hunsucker, 1982; Ding et al., 2007]. The change of the propagation direction of LSTIDs
2 as they move from high to middle latitudes during the superstorm of 29 October 2003 over North
3 America, was explained by Ding et al. [2007] as related to a change in the position of the
4 electrojet enhancement area near the auroral oval. Nevertheless, since the structure and the
5 evolution process of the source region during storm period is complicated, more cases and
6 modeling studies are needed to find a clear connection between it and the propagation direction of
7 LSTIDs.

8 In general, the velocity of the neutral wind is much less than that of the LSTIDs, and the
9 thermospheric wind velocity in the same latitudinal belt with a limited longitudinal extension
10 should exhibit little variance. So, the contribution of the background wind on the change of the
11 propagating direction would be limited in the absence of the geomagnetic field. However, a
12 combined effect of magnetic declination and zonal wind can cause F region electron density
13 differences between two sides of the zero declination [Zhang et al., 2011]. During storm periods,
14 the enhanced zonal winds [Fuller-Rowell et al., 1994] can intensify these differences [Thomas et
15 al, 2016]. As a result, the geomagnetic declination is considered to be an important factor that
16 affects the propagation direction of the LSTID. Some researchers have studied the predominant
17 propagation direction of LSTIDs during storm periods in different longitudinal sectors, and
18 suggest that, statistically speaking, the predominant directions of LSTID in Europe, China and
19 Japan are primarily southward, South to West and South to East, respectively [Nicolls et al, 2004;
20 Tsugawa et al, 2004; Borries 2009; Ding et al, 2013]. These results are all consistent with the
21 corresponding geomagnetic declination in each sector.

22 In the longitudinal region of 70°E - 150°E , the geomagnetic declination angles change from North
23 by East in the West side to North by West in the East side. This characteristic seems to show some
24 kind of consistent with the azimuth results in Table 1. To illustrate such connection quantitatively,
25 Figure 9 depicts the (a) the geomagnetic declination on the wavefront in different longitudes in
26 Figure 7 and (b) the propagation direction (azimuth- 180°) of the LSTID at the same spot. The
27 connection between these two parameters is quite obvious in this event. This result manifests that
28 the propagation of LSTIDs in different longitudes is probably influenced by the orientation of the
29 geomagnetic field lines in the East Asian sector. In addition, the tendency of field-aligned
30 propagation of the LSTID indicates that it is driven by the neutral winds since the winds push the
31 plasma up and down along the magnetic field lines. There is no evidence, such as simultaneous
32 perturbations at all latitudes in other cases [Borries et al., 2016; Zakharenkova et al., 2016], to
33 show that the LSTID in the Chinese/Japanese sector is affected by prompt penetration electric
34 field (PPEF) during the same period. Besides, considering the relatively low data coverage in the
35 East/West side of the studied region, it should be noted that our speculation needs to be verified
36 with more observational data and numerical simulation to reduce uncertainty in our propagation
37 estimation and to figure out the detailed physical processes.

38 During the 2015 St. Patrick's Day storm, LSTIDs in the European-African, American and
39 Asian-Australian sectors are detected and analysed with TEC observations [Borries et al., 2016;
40 Zakharenkova et al., 2016; Habarulema et al., 2018]. It shows clearly in their results that the
41 European sector also exhibits LSTIDs around 11:00 UT. As a comparison, we also analysed these
42 LSTIDs but with VTEC data from the Madrigal database of the MIT Haystack Observatory. This
43 database has good spatiotemporal coverage for the European and American sectors. To derive the

1 VTECP, a narrow longitudinal band (10°E - 20°E , 30°N - 70°N) is first selected and the VTEC data
2 with the same latitude at the same time is average. At each latitude bin, the averaged VTEC forms
3 a time series and the temporal resolution is reset to 12 minutes (0.2 hours) with bin averaging.
4 Then, a running mean with a 1.5 hours window is conducted for each time series and their
5 difference is taken as the VTECP. The result is plotted in Figure 10 as a TLP. The fitting lines are
6 obtained with the same method as those in Figure 8.

7 Figure 10 is basically consistent with previous results, such as the synchronous perturbations
8 around 04:45 UT and 09:15 UT, and the LSTID structures between 10:00 UT and 17:00 UT.
9 Moreover, our result shows that the VTECP' behavior between 60°N and 70°N is quite different
10 from below. The pattern around 10:00 UT seems to represent a TID with smaller phase speed.
11 Considering the physical processes are more complex in such high latitudes [Foster et al., 2014],
12 we only focus on the perturbations below 60°N . The phase speeds estimated from the most distinct
13 crest and trough are $\sim 500\pm 51$ m/s and $\sim 427\pm 55$ m/s, respectively, and the estimated period is \sim
14 4.0 ± 0.2 hours. It is clear that the appearances of the LSTIDs are different in the European and the
15 East Asian sectors during the same UT period for the same storm event. Borries et al. [2016]
16 present a detailed study on the LSTID in Europe during this storm. It is suggested that the
17 perturbation occurring around 11:00 UT is special since it is impacted by PPEF and wind at the
18 same time. Comparatively, the LSTID in the Chinese/Japanese sector seems only driven by winds.
19 This may partly account for the longitudinal difference in our results. Besides, such difference
20 may also be related to the location or structure of the Joule heating source in the auroral oval or
21 the difference of the background TEC in the two sectors. For better understanding this difference,
22 more studies on the Joule heating source are needed.

23

24 5. Summary

25 Using data from 4 GPS receiver networks (CMGN, CMONOC, GEONET, IGS), together with
26 recordings of 2 HF Doppler shift stations and 8 ionosondes, we provide comprehensive and
27 detailed observation results of the LSTIDs in the East Asian sector during the 2015 St. Patrick's
28 Day storm. The GPS receiver networks in China and Japan are combined together to produce 2D
29 VTEC perturbation maps in order to give a wider image of the LSTID structures in the East Asia.
30 As a comparison, the ionospheric disturbances in the European sector are also studied with VTEC
31 data from the Madrigal database. The propagation parameters of the LSTIDs are estimated. Main
32 results can be summarized as follows:

33 (1) A trough of LSTID occurs and propagates from high to lower latitudes during 09:40-11:20 UT,
34 which spans over 60° in longitude. It is followed by a crest of LSTID that characterized by a clear
35 tendency to dissipate starting from the East side. These features are in good agreement with
36 observations by HF Doppler shift stations and ionosondes

37 (2) The propagation orientation is almost due southward around 105°E - 115°E , and it tends to
38 slightly shift westward/eastward in the West/East part of the studied area. This is expected to be
39 influenced by the regional declination of the geomagnetic field lines.

40 (3) The propagation parameters in different longitudinal bands are estimated. These parameters
41 show certain longitudinal differences. Besides, the mean values and standard deviations of the

1 period, V_t , V_c , and wavelength are 74.8 ± 1.4 minutes, 578 ± 16 m/s, 617 ± 23 m/s, and 2691 ± 80 km,
2 respectively.

3 It should be noted that our results show certain consistency with previous works focusing on the
4 Chinese or Japanese sector for different LSTID events. Nevertheless, the longitudinal dependence
5 shown in our results should be examined further with more case studies based on large
6 longitudinal and high-resolution coverage of GPS data.

7

8

9 **Acknowledgement:**

10 We are grateful to the International GPS Services (IGS) (<ftp://cddis.gsfc.nasa.gov>). The GPS data
11 from CMONOC and CMGN networks are provided by the China Earthquake Administration
12 (CEA) and the China Meteorological Administration (CMA), respectively. The GPS data from
13 GEONET are provided by the Geographical Survey Institute, Japan. GPS TEC data products and
14 access through the Madrigal distributed data system (<http://cedar.openmadrigal.org/>) are provided
15 to the community by the Massachusetts Institute of Technology under support from the US
16 National Science Foundation grant AGS-1242204. The HF Doppler records are from the Chinese
17 Meridian Project. The ionosonde data are provided by the China Research Institute of Radio wave
18 Propagation (CRIRP). We thank the NASA/GSFC's Space Physics Data Facility's OMNIWeb
19 service (<https://spdf.gsfc.nasa.gov>) for data of the interplanetary and SYM-H parameters. This
20 research was supported by the National Natural Science Foundation of China (No. 41674157).

21

22

23

1 **References**

- 2 Afraimovich, E. L., Palamartchouk, K. S., and Perevalova, N. P.: GPS radio interferometry of
3 travelling ionospheric disturbances. *Journal of Atmospheric and Solar-Terrestrial*
4 *Physics*, 60(12), 1205-1223, 1998.
- 5 Afraimovich, E. L., Kosogorov, E. A., Leonovich, L. A., Palamartchouk, K. S., Perevalova, N. P.,
6 and Pirog, O. M.: Determining parameters of large-scale traveling ionospheric disturbances
7 of auroral origin using GPS-arrays. *Journal of Atmospheric and Solar-Terrestrial*
8 *Physics*, 62(7), 553-565, 2000.
- 9 Astafyeva, E., Zakharenkova, I., and Förster, M.: Ionospheric response to the 2015 St. Patrick's
10 Day storm: A global multi-instrumental overview. *Journal of Geophysical Research: Space*
11 *Physics*, 120(10), 9023-9037, 2015.
- 12 Balthazor, R. L. and Moffett, R. J.: Morphology of large-scale traveling atmospheric disturbances
13 in the polar thermosphere. *Journal of Geophysical Research: Space Physics*, 104(A1),
14 15-24. Borries, C., Jakowski, N., & Wilken, V. (2009). Storm induced large scale TIDs
15 observed in GPS derived TEC. *Ann. Geophys*, 27(4), 1605-1612, 1999.
- 16 Borries, C., Mahrous, A. M., Ellahouny, N. M., and Badeke, R.: Multiple ionospheric
17 perturbations during the Saint Patrick's Day storm 2015 in the European-African sector.
18 *Journal of Geophysical Research: Space Physics*, 121(11), 11-333, 2016.
- 19 Borries, C., Jakowski, N., Kauristie, K., Amm, O., Mielich, J., and Kouba, D.: On the dynamics of
20 large-scale traveling ionospheric disturbances over Europe on 20 November 2003. *Journal of*
21 *Geophysical Research: Space Physics*, 122(1), 1199-1211, 2017.
- 22 Buonsanto, M. J.: Ionospheric storms—A review. *Space Science Reviews*, 88(3-4), 563-601,
23 1999.
- 24 Cherniak, I. and Zakharenkova, I.: Large-Scale Traveling Ionospheric Disturbances Origin and
25 Propagation: Case Study of the December 2015 Geomagnetic Storm. *Space Weather*, 16(9),
26 1377-1395, 2018.
- 27 Chimonas, G.: The equatorial electrojet as a source of long period travelling ionospheric
28 disturbances. *Planetary and Space Science*, 18(4), 583-589, 1970.
- 29 Coster, A. J. and Gaposchkin, E. M.: Use of GPS pseudo-range and phase data for measurement of
30 ionospheric and tropospheric refraction. In *Institute of Navigation Satellite Division, 2nd*
31 *International Technical Meeting* (pp. 439-443), 1989.
- 32 Ding, F., Wan, W., Ning, B., and Wang, M.: Large-scale traveling ionospheric disturbances
33 observed by GPS total electron content during the magnetic storm of 29-30 October
34 2003. *Journal of Geophysical Research: Space Physics*, 112(A6), 2007.
- 35 Ding, F., Wan, W., Liu, L., Afraimovich, E. L., Voeykov, S. V., and Perevalova, N. P.: A statistical
36 study of large-scale traveling ionospheric disturbances observed by GPS TEC during major
37 magnetic storms over the years 2003–2005. *Journal of Geophysical Research: Space*
38 *Physics*, 113(A3), 2008.
- 39 Ding, F., Wan, W., Ning, B., Zhao, B., Li, Q., Zhang, R., Xiong, B., and Song, Q.:
40 Two-dimensional imaging of large-scale traveling ionospheric disturbances over China based
41 on GPS data. *Journal of Geophysical Research: Space Physics*, 117(A8), 2012.
- 42 Ding, F., Wan, W., Ning, B., Zhao, B., Li, Q., Wang, Y., Hu, L., Zhang, R., and Xiong, B.:
43 Observations of poleward-propagating large-scale traveling ionospheric disturbances in
44 southern China. In *Annales Geophysicae* (Vol. 31, No. 2, p. 377). Copernicus GmbH, 2013.

1 Ding, F., Wan, W., Li, Q., Zhang, R., Song, Q., Ning, B., Liu, L., Zhao, B., and Xiong, B.:
2 Comparative climatological study of large-scale traveling ionospheric disturbances over
3 North America and China in 2011–2012. *Journal of Geophysical Research: Space*
4 *Physics*, 119(1), 519-529, 2014.

5 Figueiredo, C. A. O. B., Wrasse, C. M., Takahashi, H., Otsuka, Y., Shiokawa, K., and Barros, D.:
6 Large-scale traveling ionospheric disturbances observed by GPS dTEC maps over North and
7 South America on Saint Patrick's Day storm in 2015. *Journal of Geophysical Research: Space*
8 *Physics*, 122(4), 4755-4763, 2017.

9 Foster, J. C., Erickson, P. J., Coster, A. J., Thaller, S., Tao, J., Wygant, J. R., and Bonnell, J. W.:
10 Storm time observations of plasmasphere erosion flux in the magnetosphere and
11 ionosphere. *Geophysical Research Letters*, 41(3), 762-768, 2014.

12 Fuller-Rowell, T. J., Codrescu, M. V., Moffett, R. J., and Quegan, S.: Response of the
13 thermosphere and ionosphere to geomagnetic storms. *Journal of Geophysical Research:*
14 *Space Physics*, 99(A3), 3893-3914, 1994.

15 Habarulema, J. B., Katamzi, Z. T., and McKinnell L.-A.: Estimating the propagation
16 characteristics of largescale traveling ionospheric disturbances using ground-based and
17 satellite data, *J. Geophys. Res. Space Physics*, 118, 7768–7782, 2013.

18 Habarulema, J. B. and Carelse, S. A.: Long-term analysis between radio occultation and ionosonde
19 peak electron density and height during geomagnetic storms. *Geophysical Research Letters*,
20 43(9), 4106-4111, 2016.

21 Habarulema, J. B., Katamzi, Z. T., and Yizengaw, E.: First observations of poleward large-scale
22 traveling ionospheric disturbances over the African sector during geomagnetic storm
23 conditions. *Journal of Geophysical Research: Space Physics*, 120(8), 6914-6929, 2015.

24 Habarulema, J. B., Katamzi, Z. T., Yizengaw, E., Yamazaki, Y., and Seemala, G.: Simultaneous
25 storm time equatorward and poleward large-scale TIDs on a global scale. *Geophysical*
26 *Research Letters*, 43(13), 6678-6686, 2016.

27 Habarulema, J. B., Yizengaw, E., Katamzi-Joseph, Z. T., Moldwin, M. B., and Buchert, S.: Storm
28 Time Global Observations of Large-Scale TIDs From Ground-Based and In Situ Satellite
29 Measurements. *Journal of Geophysical Research: Space Physics*, 123(1), 711-724, 2018.

30 Hines, C. O.: Internal atmospheric gravity waves at ionospheric heights. *Canadian Journal of*
31 *Physics*, 38(11), 1441-1481, 1960.

32 Ho, C. M., Mannucci, A. J., Lindqwister, U. J., Pi, X., and Tsurutani, B. T.: Global ionosphere
33 perturbations monitored by the worldwide GPS network. *Geophysical Research*
34 *Letters*, 23(22), 3219-3222, 1996.

35 Hocke, K. and Schlegel, K.: A review of atmospheric gravity waves and travelling ionospheric
36 disturbances: 1982-1995. In *Annales Geophysicae* (Vol. 14, No. 9, p. 917), 1996.

37 Hunsucker, R. D.: Atmospheric gravity waves generated in the high-latitude ionosphere: A
38 review. *Reviews of Geophysics*, 20(2), 293-315, 1982.

39 Jonah, O. F., Coster, A., Zhang, S., Goncharenko, L., Erickson, P. J., Paula, E. R., and Kherani, E.
40 A.: TID observations and source analysis during the 2017 Memorial Day weekend
41 geomagnetic storm over North America. *Journal of Geophysical Research: Space Physics*,
42 123, 8749– 8765. <https://doi.org/10.1029/2018JA025367>, 2018.

43 Klausner, V., Fagundes, P. R., Sahai, Y., Wrasse, C. M., Pillat, V. G., and Becker-Guedes, F.:
44 Observations of GW/TID oscillations in the F2 layer at low latitude during high and low

1 solar activity, geomagnetic quiet and disturbed periods. *Journal of Geophysical Research: Space Physics*, 114(A2), 2009.

2

3 Klobuchar, J. A.: Design and characteristics of the GPS ionospheric time delay algorithm for
4 single frequency users. In *PLANS'86-Position Location and Navigation Symposium* (pp.
5 280-286), 1986.

6 Krankowski, A., Zakharenkova, I., Krypiak-Gregorczyk, A., Shagimuratov, I. I., and Wielgosz, P.:
7 Ionospheric electron density observed by FORMOSAT-3/COSMIC over the European region
8 and validated by ionosonde data. *Journal of Geodesy*, 85(12), 949-964, 2011.

9 Lanyi, G. E. and Roth, T.: A comparison of mapped and measured total ionospheric electron
10 content using global positioning system and beacon satellite observations. *Radio
11 Science*, 23(4), 483-492, 1988.

12 Lyons, L. R., Nishimura, Y., Zhang, S. R., Coster, A. J., Bhatt, A., Kendall, E., and Deng, Y.:
13 Identification of Auroral Zone Activity Driving Large-Scale Traveling Ionospheric
14 Disturbances. *Journal of Geophysical Research: Space Physics*, 124(1), 700-714, 2019.

15 Maeda, S. and Handa, S.: Transmission of large-scale TIDs in the ionospheric F2-region. *Journal
16 of Atmospheric and Terrestrial Physics*, 42(9-10), 853-859, 1980.

17 Mendillo, M. and Narvaez, C.: Ionospheric storms at geophysically-equivalent sites–Part 1:
18 Storm-time patterns for sub-auroral ionospheres. In *Annales Geophysicae* (Vol. 27, No. 4, pp.
19 1679-1694). Copernicus GmbH, 2009.

20 Morton, F. W. and Essex, E. A.: Gravity wave observations at a southern hemisphere mid-latitude
21 station using the total electron content technique. *Journal of Atmospheric and Terrestrial
22 Physics*, 40(10-11), 1113-1122, 1978.

23 Nicolls, M. J., Kelley, M. C., Coster, A. J., González, S. A., and Makela, J. J.: Imaging the
24 structure of a large-scale TID using ISR and TEC data. *Geophysical Research Letters*, 31(9),
25 2004.

26 Pederick, L. H., Cervera, M. A., and Harris, T. J.: Interpreting observations of large-scale traveling
27 ionospheric disturbances by ionospheric sounders. *Journal of Geophysical Research: Space
28 Physics*, 122(12), 2017.

29 Pradipta, R., Valladares, C. E., Carter, B. A., and Doherty, P. H.: Interhemispheric propagation and
30 interactions of auroral traveling ionospheric disturbances near the equator. *Journal of
31 Geophysical Research: Space Physics*, 121(3), 2462-2474, 2016.

32 Ramsingh, Sripathi, S., Sreekumar, S., Banola, S., Emperumal, K., Tiwari, P., and Kumar, B. S.:
33 Low-latitude ionosphere response to super geomagnetic storm of 17/18 March 2015: Results
34 from a chain of ground-based observations over Indian sector. *Journal of Geophysical
35 Research: Space Physics*, 120(12), 10-864, 2015.

36 Richmond, A. D. and Roble, R. G.: Dynamic effects of aurora-generated gravity waves on the
37 mid-latitude ionosphere. *Journal of Atmospheric and Terrestrial Physics*, 41(7-8), 841-852,
38 1979.

39 Rideout, W. and Coster, A.: Automated GPS processing for global total electron content data. *GPS
40 Solutions*, 10(3), 219-228, 2006.

41 Saito, A., Fukao, S., and Miyazaki, S.: High resolution mapping of TEC perturbations with the
42 GSI GPS network over Japan. *Geophysical research letters*, 25(16), 3079-3082, 1998.

43 Saito, A., Nishimura, M., Yamamoto, M., Fukao, S., Kubota, M., Shiokawa, K., Otsuka, Y.,
44 Tsugawa, T., Ogawa, T., Ishii, M., Sakanoi, and T., Miyazaki, S.: Traveling ionospheric

1 disturbances detected in the FRONT campaign. *Geophysical Research Letters*, 28(4),
2 689-692, 2001.

3 Shiokawa, K., Otsuka, Y., Ogawa, T., Balan, N., Igarashi, K., Ridley, A. J., Knipp, D. J., Saito, A.,
4 and Yumoto, K.: A large-scale traveling ionospheric disturbance during the magnetic storm of
5 15 September 1999. *Journal of Geophysical Research: Space Physics*, 107(A6), SIA-5, 2002.

6 Song, Q., Ding, F., Wan, W., Ning, B., Liu, L., Zhao, B., Li, Q., and Zhang, R.: Statistical study of
7 large-scale traveling ionospheric disturbances generated by the solar terminator over
8 China. *Journal of Geophysical Research: Space Physics*, 118(7), 4583-4593, 2013.

9 Thomas, E. G., Baker, J. B. H., Ruohoniemi, J. M., Coster, A. J., and Zhang, S. R.: The
10 geomagnetic storm time response of GPS total electron content in the North American
11 sector. *Journal of Geophysical Research: Space Physics*, 121(2), 1744-1759, 2016.

12 Tsugawa, T., Saito, A., Otsuka, Y., and Yamamoto, M.: Damping of large-scale traveling
13 ionospheric disturbances detected with GPS networks during the geomagnetic storm. *Journal*
14 *of Geophysical Research: Space Physics*, 108(A3), 2003.

15 Tsugawa, T., Saito, A., and Otsuka, Y.: A statistical study of large-scale traveling ionospheric
16 disturbances using the GPS network in Japan. *Journal of Geophysical Research: Space*
17 *Physics*, 109(A6), 2004.

18 Tsugawa, T., Shiokawa, K., Otsuka, Y., Ogawa, T., Saito, A., and Nishioka, M.: Geomagnetic
19 conjugate observations of large-scale traveling ionospheric disturbances using GPS networks
20 in Japan and Australia. *Journal of Geophysical Research: Space Physics*, 111(A2), 2006.

21 Wan, W., Ning, B., Yuan, H., Li, J., Li, L., and Liang, J.: TID observation using a short baseline
22 network of GPS receivers. *Acta Geodaetica et Geophysica Hungarica*, 32(3-4), 321-327,
23 1997.

24 Wang, C.: New Chains of Space Weather Monitoring Stations in China, *Space*
25 *Weather*, 8, S08001, doi:10.1029/2010SW000603, 2010.

26 Zakharenkova, I., Astafyeva, E., and Cherniak, I.: GPS and GLONASS observations of large-scale
27 traveling ionospheric disturbances during the 2015 St. Patrick's Day storm. *Journal of*
28 *Geophysical Research: Space Physics*, 121(12), 2016.

29 Zhang, D. H. and Xiao, Z.: Study of ionospheric response to the 4B flare on 28 October 2003
30 using International GPS Service network data. *Journal of Geophysical Research: Space*
31 *Physics*, 110(A3), 2005.

32 Zhang, D. H., Zhang, W., Li, Q., Shi, L. Q., Hao, Y. Q., and Xiao, Z.: Accuracy analysis of the
33 GPS instrumental bias estimated from observations in middle and low latitudes. In *Annales*
34 *Geophysicae* (Vol. 28, No. 8, pp. 1571-1580). Copernicus GmbH, 2010.

35 Zhang, S. R., Foster, J. C., Coster, A. J., and Erickson, P. J.: East-West Coast differences in total
36 electron content over the continental US. *Geophysical Research Letters*, 38(19), 2011.

37 Zhang, S. R., Erickson, P. J., Goncharenko, L. P., Coster, A. J., Rideout, W., and Vierinen, J.:
38 Ionospheric bow waves and perturbations induced by the 21 August 2017 solar
39 eclipse. *Geophysical Research Letters*, 44(24), 12-067, 2017.

40 Zhang, W., Zhang, D. H., and Xiao, Z.: The influence of geo-magnetic storms on the estimation of
41 GPS instrumental biases, *Ann. Geophys.*, 27, 1613-1623, doi:10.5194/angeo-27-1613-2009,
42 2009.

43

1 **Captions of Table and Figures**

2 **Table 1.** The estimated propagation parameters of the LSTID and the corresponding standard
3 errors. The second column contains the propagation directions, which are measured clockwise
4 from the South. V_t/V_c represents the phase speed estimated with certain wave trough/crest.

5 **Figure 1.** Locations of the GPS stations of different networks (colored dots), the HF Doppler shift
6 stations (green stars), the National Time Service Center of China (grey stars), and the ionosondes
7 (green triangles) that used in this study.

8 **Figure 2.** Temporal variations of (a) the solar wind speed (V_{sw}), (b) the IMF Bz component, (c)
9 the SYM-H index, and (d) the AE index between 18:00 UT, 16 March 2015 and 06:00 UT, 18
10 March 2015. The occurrence of SSC is shown with vertical dashed lines.

11 **Figure 3.** Temporal variations of the HF Doppler shift records from (a) MDT and (b) SZT
12 between 08:00 UT and 14:00 UT, 17 March 2015.

13 **Figure 4.** A series of 2D VTECP' maps over the East Asian sector from the period of 09:40-09:50
14 UT to 11:30-11:40 UT on 17 March 2015. The grey areas represent the nightside. The colorbar
15 represents the VTECP' (units: TECu), which is transformed from the original VTECP value with
16 equation (3) for a more viewer-friendly colormap. The green and yellow lines illustrate the least
17 square fittings (order 2) for wavefronts.

18 **Figure 5.** Temporal variations of mean VTECP' near the Doppler reflection points between 08:00
19 UT and 14:00 UT, 17 March 2015. Doppler shift recordings in Figure 3 are plotted with dashed
20 lines for comparison.

21 **Figure 6.** Temporal variations of the virtual height for iso-frequency lines from 8 ionosondes
22 between 08:00 UT and 12:00 UT, 17 March 2015. Frequencies are depicted on each iso-frequency
23 line. The time resolution is 15 min for all stations. The black dashed lines indicate the downward
24 phase change.

25 **Figure 7.** A detailed example of the wavefront fitting method. Green dots indicate the data points
26 for least square fitting. Green arrows depict the propagation orientations in different longitudes.
27 Dashed black rectangles mark the areas for generating TLPs in Figure 8.

28 **Figure 8.** TLPs of VTECP' for different longitudinal bands between 07:00-14:00 UT. White dots
29 give the data points for linear fitting, and the fitting results are marked with white lines. 30°N in
30 (b-d, f) is marked with black dashed lines which indicate the boundary of EIA. 40°N is marked in
31 (f).

32 **Figure 9.** The sketch of (upper) the geomagnetic declination angels and (lower) the propagation
33 directions in different longitudes on the wavefront fitted in Figure 7. The propagation directions
34 are measured clockwise from the South.

35 **Figure 10.** The TLP of VTECP' for the European sector (10°E-20°E, 30°N-70°N) between
36 01:00-23:00 UT. White lines and dots are similar to those in Figure 8. The black dashed line
37 depicts 60°N.

38

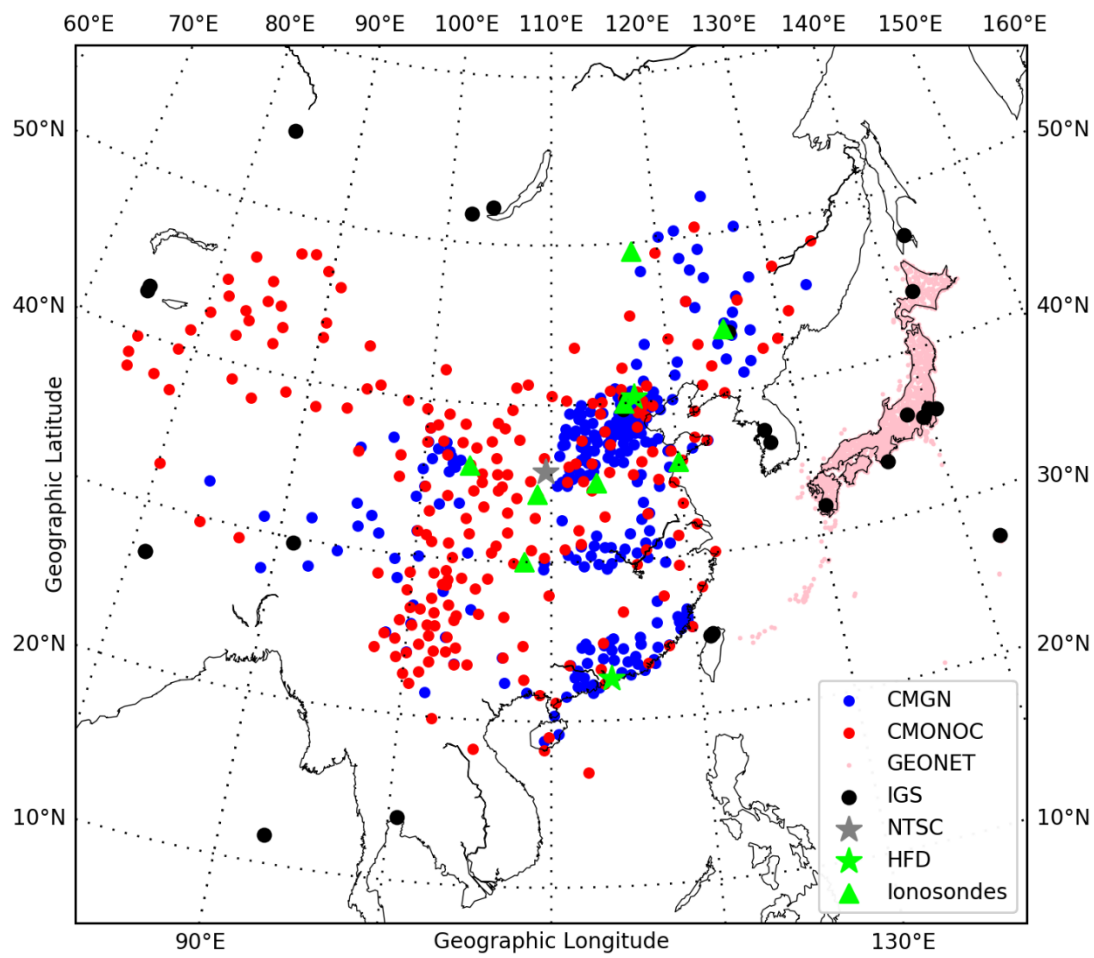
1 **Table 1.**

Lon. (°E)	Dir. (°)	Period (min)	Vt (m/s)	Vc (m/s)	Wavelength (km)
80-90	-11.2	81.1±3.4	500±40	542±31	2536±163
90-100	-7.1	77.6±5.2	552±22	670±44	2845±222
100-110	-2.9	58.8±1.5	587±47	638±76	2160±167
110-120	1.3	62.4±2.0	605±27	562±25	2184±99
120-130	7.9	94.2±1.3	647±39	673±63	3731±216

2

3

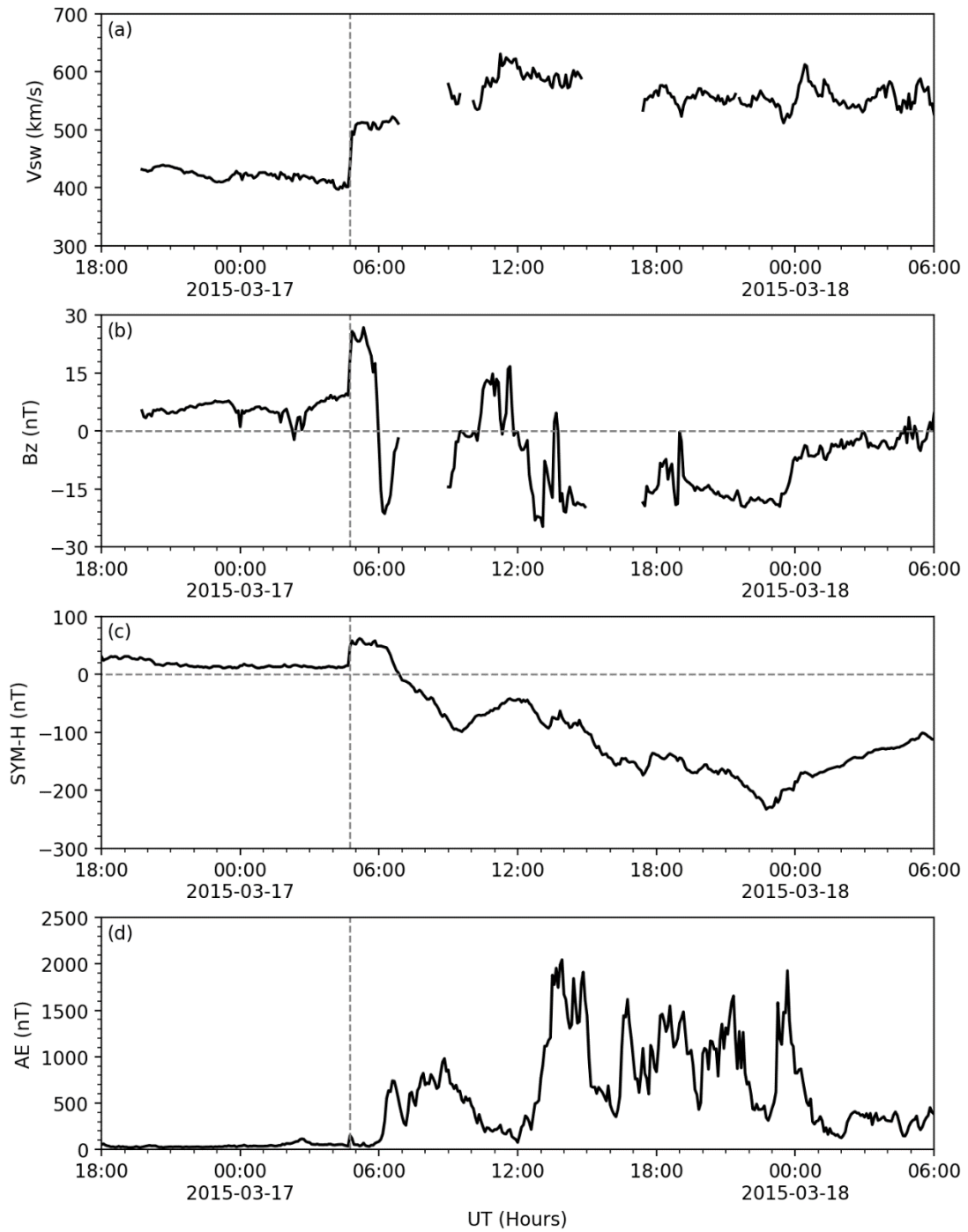
1 Figure 1.



2

3

1 Figure 2.

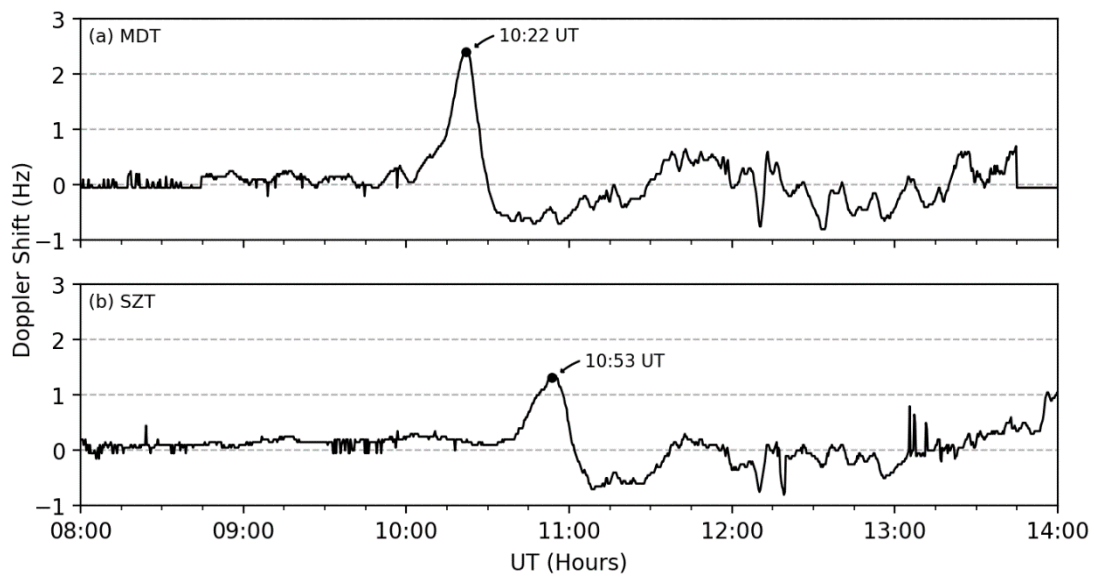


2

3

4

1 Figure 3.



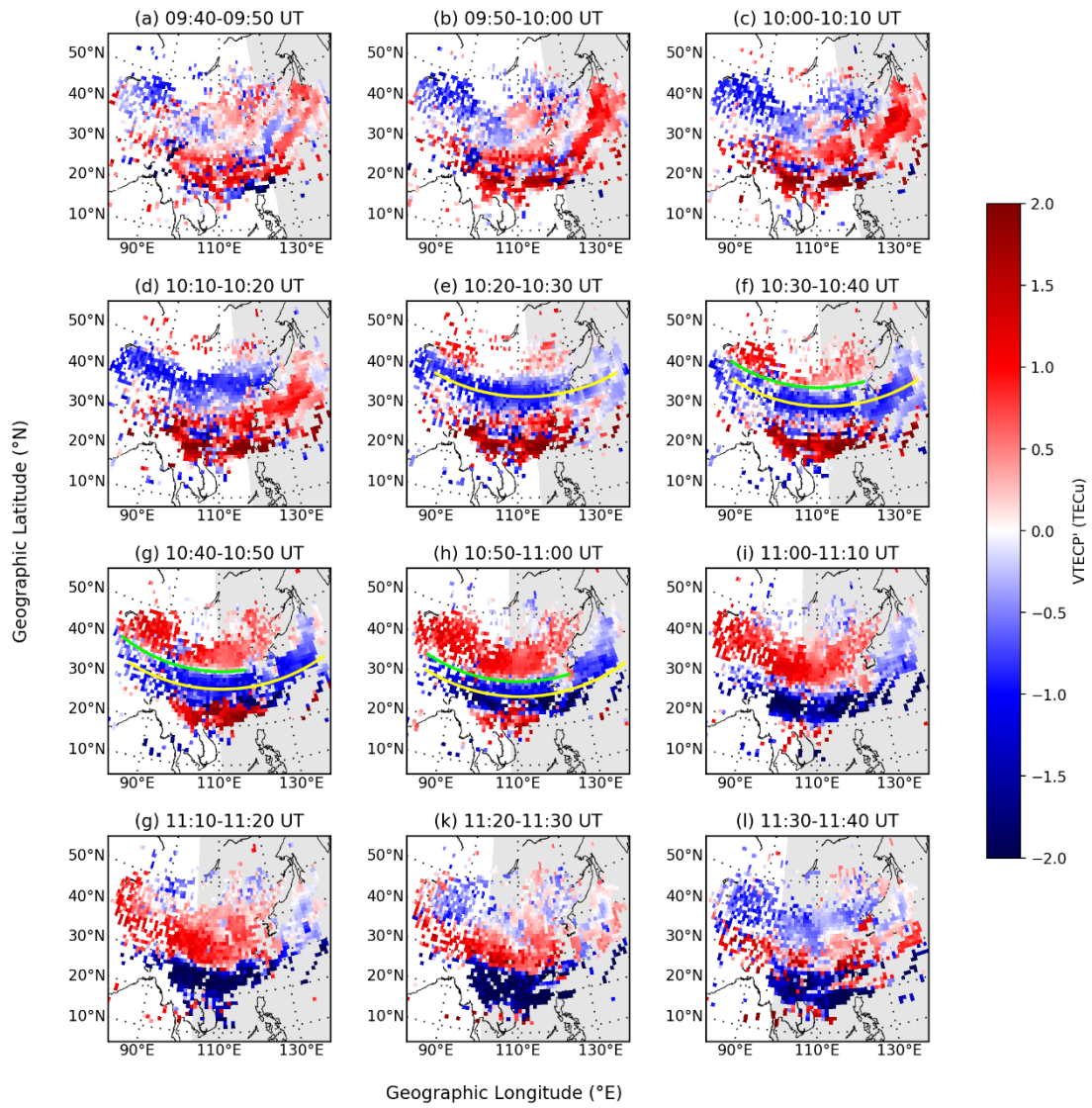
2

3

4

5

1 Figure 4.

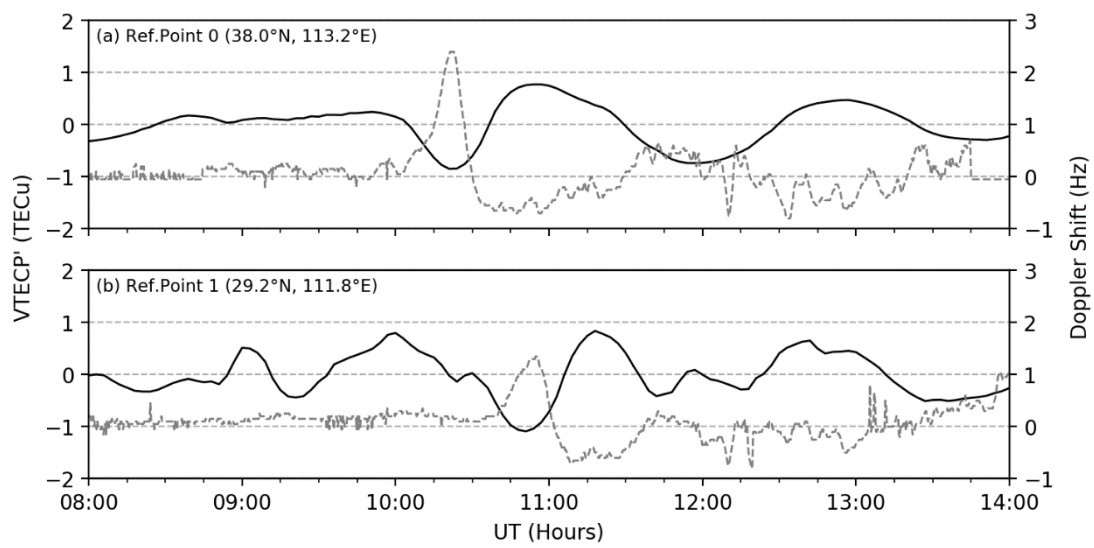


2

3

4

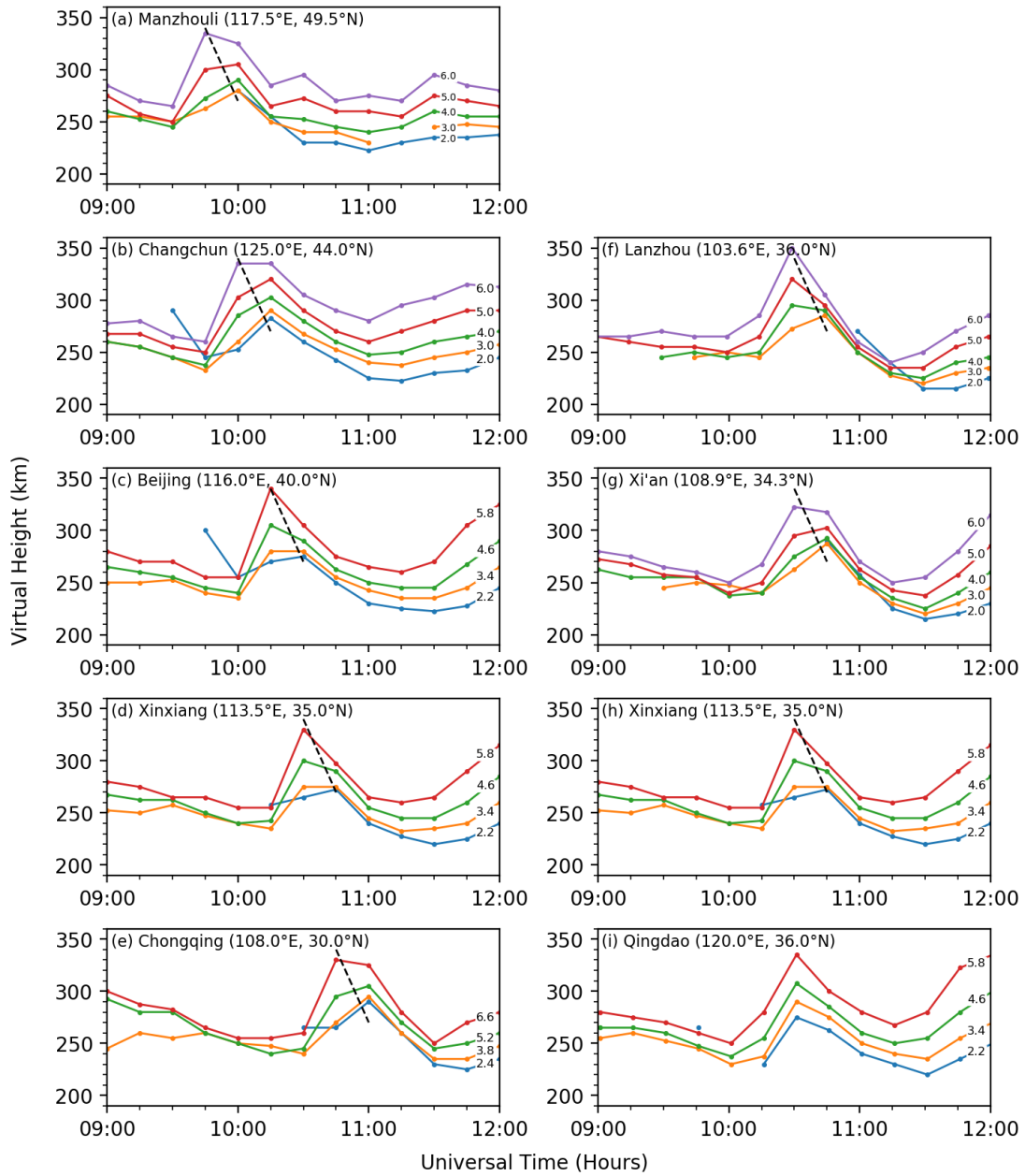
1 Figure 5.



2

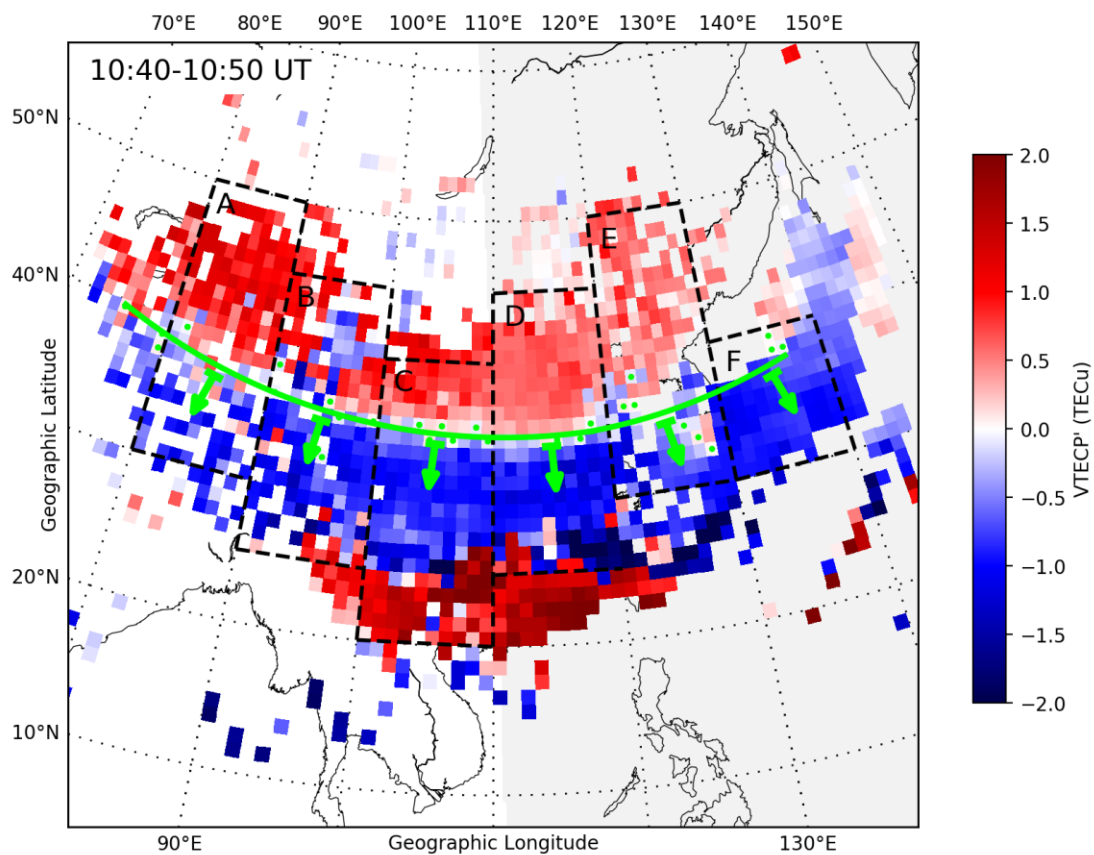
3

1 Figure 6.



2
3

1 Figure 7.



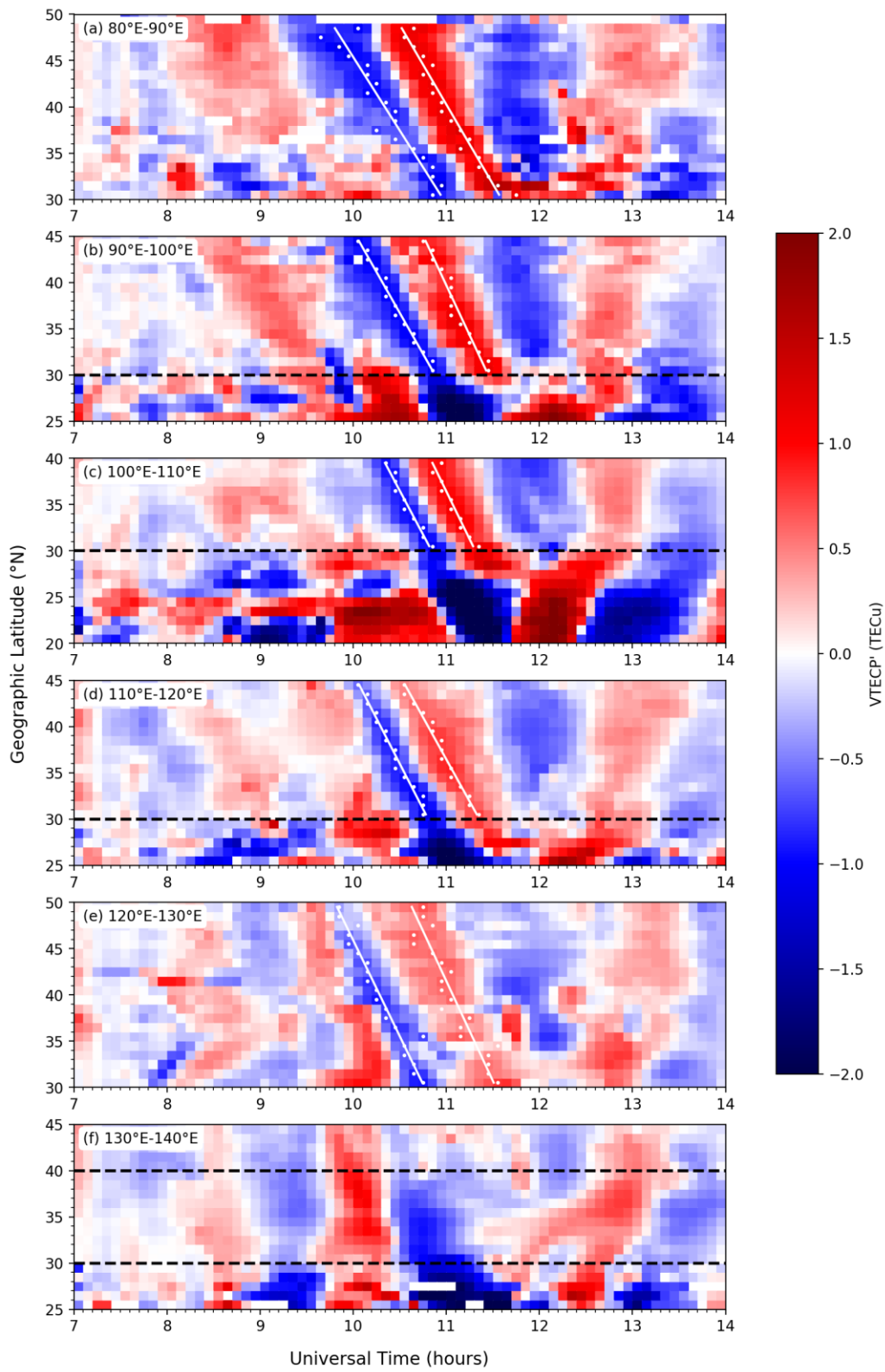
2

3

4

5

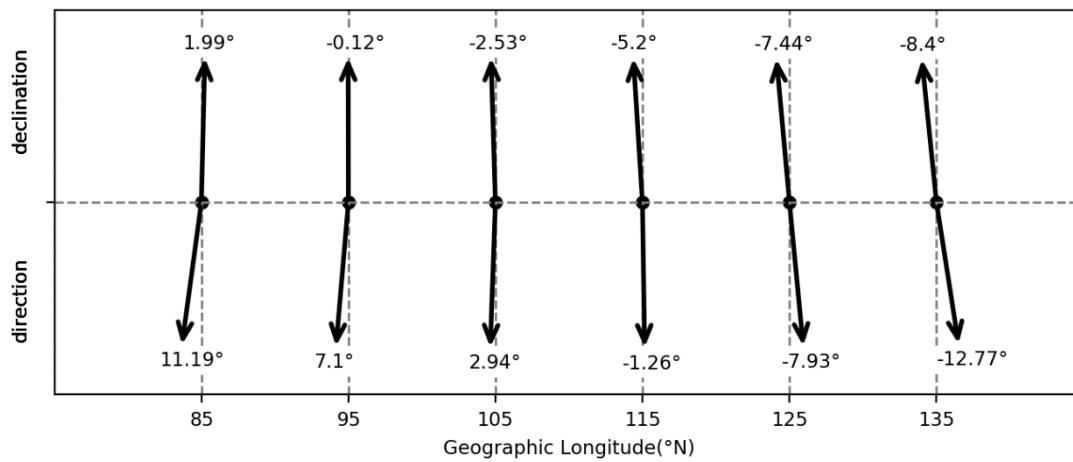
1 Figure 8.



2

3

1 Figure 9.

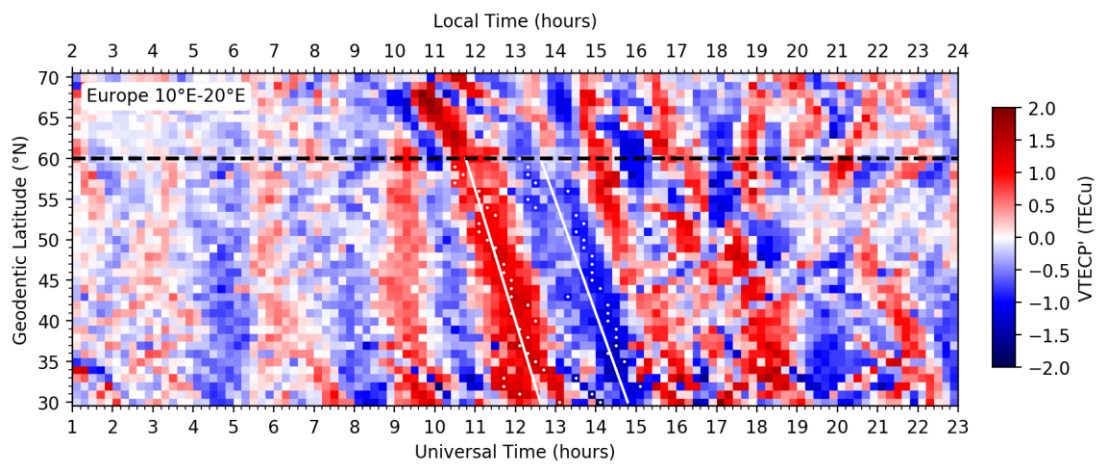


2

3

4

1 Figure 10.



2

3

4